Siberian carbon sink reduced by forest disturbances

Lei Fan, Jean-Pierre Wigneron, Philippe Ciais, Jérome Chave, Martin Brandt, Stephen Sitch, Chao Yue, Ana Bastos, Xin Li, Yuanwei Qin, et al.

Siberian carbon sink reduced by forest disturbances

Lei Fan[1], Jean-Pierre Wigneron[2,3], Philippe Ciais[4], Jérome Chave[5], Martin Brandt [6], Stephen Sitch[7], Chao Yue[8], Ana Bastos[9], Xin Li[10], Yuanwei Qin[11], Wenping Yuan [12], Dmitry Schepaschenko[13,14,15], Liudmila Mukhortova[14], Xiaojun Li[2,3], Xiangzhuo Liu[2,3], Mengjia Wang [2], Frédéric Frappart [2,3], Xiangming Xiao [11], Jingming Chen[16], Mingguo Ma [1], Jianguang Wen[17], Xiuzhi Chen[12], Hui Yang[9], Dave van Wees [18] & Rasmus Fensholt [6]

[1] Chongqing Jinfo Mountain Karst Ecosystem National Observation and Research Station, School of Geographical Sciences, Southwest University, Chongqing, China.
[2] INRAE, Bordeaux Sciences Agro, UMR 1391 ISPA, Villenave-d'Ornon, France.
[3] Université de Bordeaux, Talence, France.
[4] Laboratoire des Sciences du Climat et de l'Environnement, LSCE/IPSL, CEA-CNRS-UVSQ, Université Paris-Saclay, Gif-sur-Yvette, France.
[5] Laboratoire Evolution and Diversité Biologique, CNRS, IRD, UT3, Université Paul Sabatier, Toulouse, France.
[6] Department of Geosciences and Natural Resource Management, University of Copenhagen, Copenhagen, Denmark.
[7] College of Life and Environmental Sciences, University of Exeter, Exeter, UK.
[8] State Key Laboratory of Soil Erosion and Dryland Farming on the Loess Plateau, Northwest A&F University, Yangling, China.
[9] Department of Biogeochemical Integration, Max Planck Institute for Biogeochemistry, Jena, Germany.
[10] National Tibetan Plateau Data Center (TPDC), State Key Laboratory of Tibetan Plateau Earth System, Environment and Resources (TPESER), Institute of Tibetan Plateau Research, Chinese Academy of Sciences, Beijing, China.
[11] Department of Microbiology and Plant Biology, Center for Earth Observation and Modeling, University of Oklahoma, Norman, OK, USA.
[12] Guangdong Province Key Laboratory for Climate Change and Natural Disaster Studies, School of Atmospheric Sciences, Sun Yat-sen University, Guangzhou, China.
[13] International Institute for Applied Systems Analysis, Laxenburg, Austria.
[14] V.N. Sukachev Institute of Forest, Siberian Branch of the Russian Academy of Science, Krasnoyarsk, Russia.
[15] Siberian Federal University, Krasnoyarsk, Russia.
[16] Department of Geography and Program in Planning, University of Toronto, Toronto, Ontario, Canada.
[17] State Key Laboratory of Remote Sensing Science, Aerospace Information Research Institute, Chinese Academy of Sciences, Beijing, China.
[18] Department of Earth Sciences, Vrije Universiteit, Amsterdam, the Netherlands.

Abstract. Siberian forests are generally thought to have acted as an important carbon sink over recent decades, but exposure to severe droughts and fire disturbances may have impacted their carbon dynamics. Limited available forest inventories mean the carbon balance remains uncertain. Here we analyse annual live and dead above-ground carbon changes derived from low-frequency passive microwave observations from 2010 to 2019. We find that during this period, the carbon balance of Siberian forests was close to neutral, with the forests acting as a small carbon sink of $+0.02^{+0.03}_{+0.01}$ PgC yr^{-1}. Carbon storage in dead wood increased, but this was largely offset by a decrease in live biomass. Substantial losses of live above-ground carbon are attributed to fire and drought, such as the widespread fires in northern Siberia in 2012 and extreme drought in eastern Siberia in 2015. These live above-ground carbon losses contrast with 'greening' trends seen in leaf area index over the same period, a decoupling explained by faster post-disturbance recovery of leaf area than live above-ground carbon. Our study highlights the vulnerability of large forest carbon stores in Siberia to climate-induced disturbances, challenging the persistence of the carbon sink in this region of the globe.

Siberia holds about 20% of the world's forest areas [1], and the region has been exposed to rapid warming in recent decades [2]. In response to warmer temperatures, a longer growing season [3] and widespread 'greening' seen by optical remote-sensing data [4,5] have been reported. These changes are generally interpreted as increases in above-ground biomass carbon (AGC) [6] and CO2 uptake [7,8], and the prevailing view is that Siberian forests have acted as a net sink for atmospheric CO2 during recent decades [9–13].

However, the shift to a drier climate with an increasing frequency of wildfires [14] causing forest loss and degradation may have weakened the carbon sink of Siberian forests [15]. Wildfires make up the largest proportion of forest loss in Siberia [16,17], causing significant carbon emissions (from live biomass and dead wood) [18] and already resulting in parts of Siberia emitting more carbon than is being captured [19,20]. A divergence between the trends of warming and greening has also been observed in Siberia [21], with localized shifts to a negative relationship between temperature and

https://doi.org/10.1038/s41561-022-01087-x

greenness indices, especially in drought-affected areas [22]. Recent heatwaves and wildfire events in 2010, 2012 and 2015 may change the carbon balance of the Siberian forest.

In the recent decade, a direct spatially explicit quantification of the carbon budget of the Siberian forests is still lacking, with varying estimates of carbon fluxes (+0.5 to −0.4 PgC yr^{-1}; positive values indicate net carbon increase in above-ground biomass) from forest inventories [23], dynamic global vegetation models [19,24] and atmospheric inversions [25,26]. Observational forest monitoring data are scarce, given the lack of systematic forest inventories in this region [14,27]. Greening trends are observed in the Siberian forests from optical satellite observations5, but the use of those indices at the high latitudes is complex [28]. In particular, variations of greenness caused by sun angle [29] and shadow effects [30] cause large differences between satellite products [31], and greenness indices saturate even at moderate biomass in the high latitudes [28]. These uncertainties impede a full understanding on how drought and wildfire influenced the spatial patterns of loss and post-disturbance recovery of forest carbon.

In this Article, we estimate wall-to-wall annual changes in the above-ground biomass carbon stocks, the sum of living biomass and dead wood, over Siberian forests from 2010 to 2019 (Fig. 1a). We present the following: (1) changes in regional AGC; (2) the relative contributions of wildfire and other forest-loss drivers to AGC loss; and (3) the decoupling between AGC and greenness trends. Spatially explicit live above-ground biomass carbon (AGC_{live}) at 25 km spatial resolution was computed using L-band vegetation optical depth (L-VOD) from passive microwave observations, which is sensitive to the biomass of stems, branches and leaves and does not saturate even in dense forests [32]. Moreover, L-VOD is not sensitive to the effects of sun illumination and atmosphere (aerosols, clouds), which limit the capabilities of optical observations at high latitudes [28].

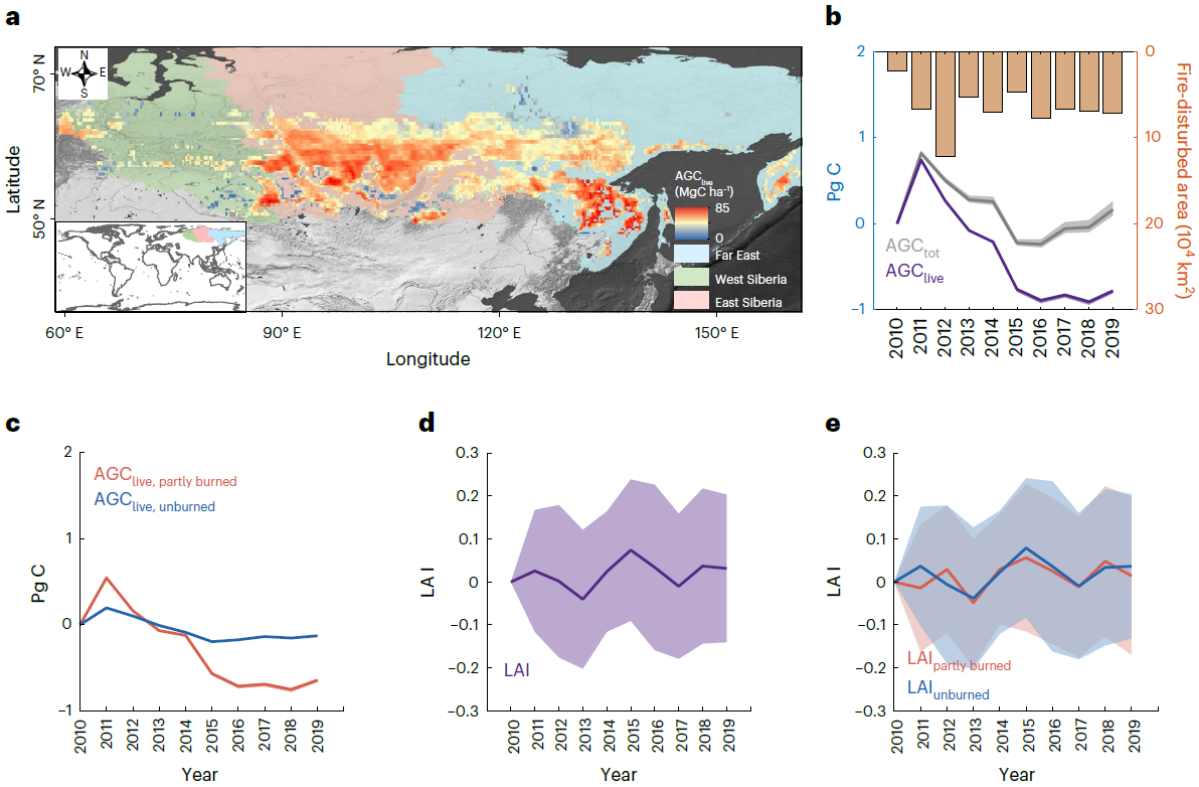

Fig. 1. Temporal variations in annual AGC and LAI over Siberian forests. **a**, The spatial distribution of AGC_{live} in 2010 (n = 6,419). **b**, Annual values of AGC_{tot} and AGC_{live} stocks (n = 10) relative to those in 2010, respectively. **c,e**, Corresponding changes in AGC_{live} (c) and LAI (e) are shown for partly burned and unburned regions. **d**, Annual values of LAI (n = 10) relative to LAI in 2010. The ranges in **b** and **c** where represented by shading around the line show the minimum and maximum of above-ground carbon changes. The centre lines and the shading ranges in **d** and **e** represent the median values and one standard deviation. Annual fire-disturbed areas are indicated by the orange bar.

https://doi.org/10.1038/s41561-022-01087-x

Above-ground carbon changes in the Siberian forests

For the years 2010–2019, we found a net AGC_{live} change in Siberia of $-0.08^{-0.08}_{-0.08}$ PgC yr^{-1} (range from calibrations of L-VOD against six different static biomass maps; Fig. 1b). This net change represents a balance between regional and temporal gross gains ($+0.29^{+0.31}_{+0.29}$ PgC yr^{-1}) offset by on average larger gross losses ($-0.37^{-0.36}_{-0.39}$ PgC yr^{-1}). Western Siberia had a nearly neutral carbon balance, while East Siberia and the Far East forests showed net carbon losses ($-0.03^{-0.03}_{-0.03}$ PgC yr^{-1} and $-0.05^{-0.05}_{-0.05}$ PgC yr^{-1}, respectively) (Supplementary Fig. 1).

Annual changes in AGC_{live} reached maximum values ($-0.74^{-0.77}_{-0.72}$ PgC) in 2011, mainly from East Siberia ($-0.49^{-0.50}_{-0.48}$ PgC), and decreased steadily afterwards (Fig. 1b and Supplementary Fig. 1). During the drought and heatwave of summer 2012, Hansen et al.[33] reported a forest area loss of 3.8 × 10^4 km^2 and record-breaking wildfires (1.2 × 10^5 km^2) as monitored by the active fire data34 (Fig. 1b). This event is associated with a change in AGC_{live} of $-0.48^{-0.47}_{-0.50}$ PgC that year, including $-0.22^{-0.22}_{-0.23}$ PgC in East Siberia and $-0.26^{-0.26}_{-0.26}$ PgC in the Far East (Supplementary Fig. 1). We found the largest decline in AGC_{live} of the decade in 2015, a net change of $-0.55^{-0.54}_{-0.57}$ PgC, of which $-0.30^{-0.30}_{-0.30}$ PgC occurred in East Siberia (Supplementary Fig. 1c) and $-0.22^{-0.21}_{-0.22}$ in the Far East (Supplementary Fig. 1e), partly attributed to extreme hot and dry conditions, 2015 being the hottest year on record since 1936 (Supplementary Fig. 2a) [35].

Drought conditions persisted until 2017 over East Siberia, indicated by negative anomalies in soil moisture and Standardized Precipitation Evapotranspiration Index (SPEI) values (Supplementary Figs. 2c and 3–5). This persistent drought was associated with continuing large wildfires (6.1 × 10^4 km^2) in 2016 and in 2017 (4.1×10^4 km^2) that contributed to the continuous decrease of AGC_{live} in East Siberia during 2015–2017 (Supplementary Fig. 1c). During that period, a contrasting vegetation response emerged from optical time-series imagery, with positive anomalies shown by leaf area index (LAI) values (Supplementary Fig. 3–5). LAI had in fact maximum values during the dry and hot year of 2015 (Supplementary Fig. 6c), as documented by Bastos et al. [36].

It is important to note here that AGC_{live} losses in a given year due to stand-replacing fires do not cause only an instantaneous CO2 emission to the atmosphere, but also at first an increase of the carbon stocks of dead wood (for example, coarse woody debris (CWD)) followed by a lagged CO2 emission from decaying CWD and litter pools [37]. Such an increase in CWD carbon (CWDC) stocks following stand-replacing fires is of particular importance for Siberian forests [38], where the combustion completeness of live biomass can be as low as 10% (Supplementary Table 5), meaning that the rest is feeding the CWDC pools. Ignoring fine litter changes, we estimated carbon changes from above-ground CWD, separating previously accumulated CWDC before the beginning of the L-VOD records in 2010 and the formation of new CWDC caused by stand-replacing fire and background mortality after 2010 (Methods and Supplementary Text). Then we calculated the total AGC (AGC_{tot}) changes accounting for AGC_{live} and CWDC (Fig. 1b).

During 2010–2019, AGCtot shows a net change of $+0.02^{+0.03}_{+0.01}$ PgC yr^{-1} (Fig. 1b), corresponding to a nearly neutral carbon balance, so that the large increase in carbon stocks of CWD ($+0.10^{+0.11}_{+0.09}$ PgC yr^{-1}) has nearly offset the decrease of AGC_{live}. Comparing decadal trends of AGC_{tot} with AGC_{live}, AGC_{tot} had a small negative trend during 2011–2015 but a rapid increase during 2015–2019, whereas AGC_{live} remained flat, ~0.8 PgC below its value in 2010 (Fig. 1b). Differences between the net changes in AGC_{tot} and AGC_{live} were observed mainly over East Siberia ($+0.02^{+0.02}_{+0.02}$ PgC yr^{-1} versus $-0.03^{-0.03}_{-0.03}$ PgC yr^{-1}) and Far East ($-0.01^{-0.01}_{-0.02}$ PgC yr^{-1} versus $-0.05^{-0.05}_{-0.05}$ PgC yr^{-1}) (Supplementary Fig. 1). The gross carbon loss is lower for AGC_{tot} ($-0.33^{-0.33}_{-0.34}$ PgC yr^{-1}) than for AGC_{live} ($-0.37^{-0.36}_{-0.39}$ PgC yr^{-1}) due to carbon remaining in CWD after mortality. Spatially, the region-wide increase in the accumulation in carbon stocks of CWD (Fig. 2c) offset 31% of AGC_{live} loss areas (Fig. 2b), resulting in 54% of the study area acting as a C sink during 2010–2019 (Fig. 2a).

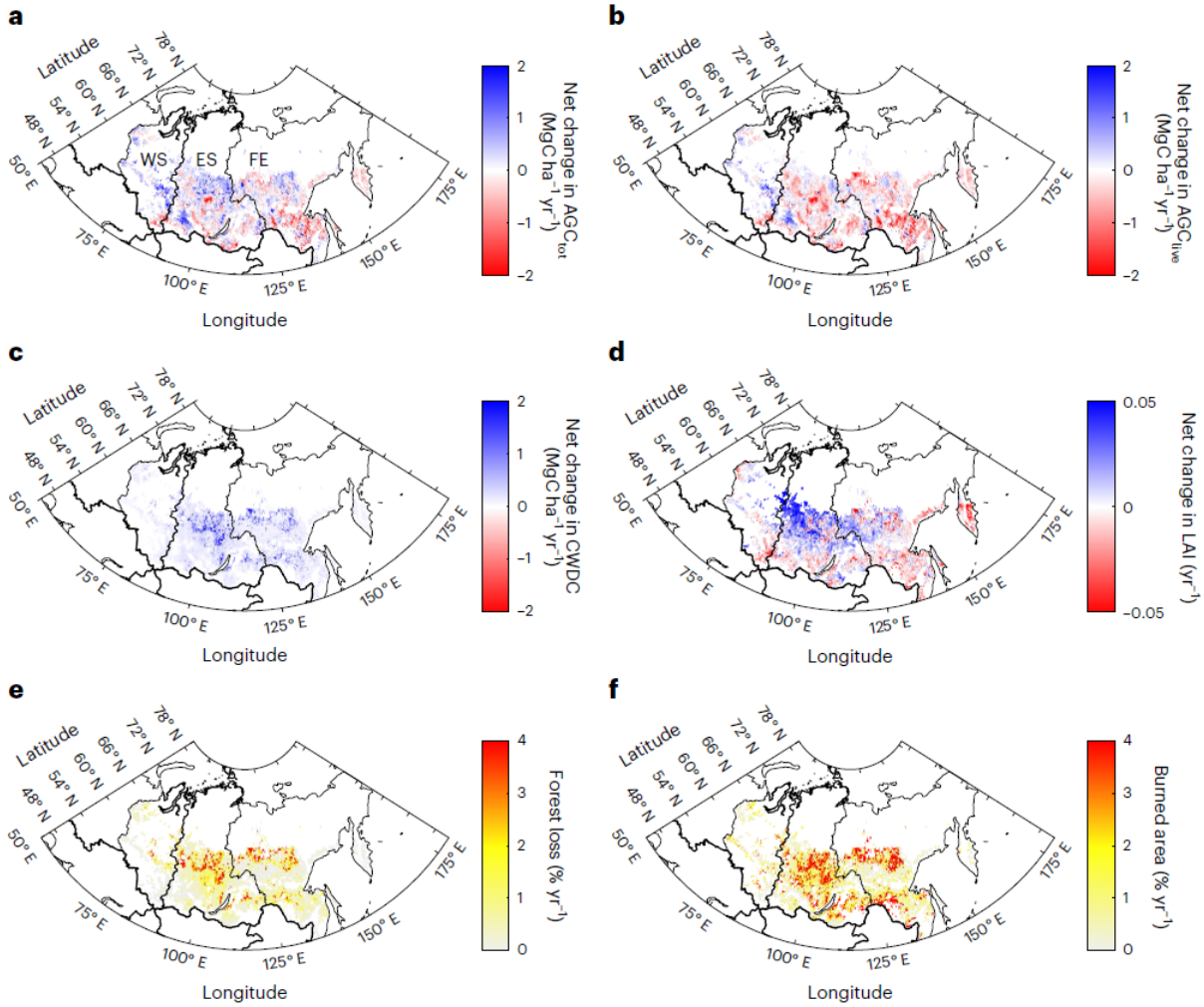

Fig. 2. Spatial patterns of net changes in AGC, CWDC and LAI. **a–d**, Net changes in AGC_{tot} (**a**), AGC_{live} (**b**), CWDC (**c**) and LAI (**d**). **e,f**, Yearly changes in forest loss (**e**) and burned area (**f**) were estimated using the Hansen [33] and moderate-resolution imaging spectroradiometer datasets, respectively. WS, West Siberia region; ES, East Siberia region; FE, Far East region. (n = 6,419 for **a–f**).

Carbon losses from forest loss and degradation

The AGC_{live} decrease in Siberian forests can be due to forest area loss from human-induced deforestation plus stand-replacing fires and other severe disturbances such as windstorms and massive insect outbreaks, and to 'degradation' processes that do not lead to forest area loss such as low-intensity fires, selective logging, fragmentation and edge effects, and partial mortality from moderate- and low-intensity disturbances such as droughts [39]. The contributions of forest area loss and degradation to AGC_{live} losses were separated within each 25 km grid cell using the method of Harris et al. [40] and Qin et al. [41]. To do so, we used the Landsat forest area loss data from ref. 33 at 30 m resolution, which means that small-scale forest area loss that is not resolved at this resolution is implicitly treated as degradation (Methods). Of the gross AGC_{live} losses ($-0.36^{-0.36}_{-0.39}$ PgC yr^{-1}) during 2010–2019, we attributed ~43% ($-0.16^{-0.14}_{-0.18}$ PgC yr^{-1}) to forest area loss and the remaining ~57% ($-0.21^{-0.21}_{-0.22}$ PgC yr^{-1}) to degradation, showing that degradation brings an even larger contribution than forest area loss.

Over the forest area loss regions, we further separated the contributions of clearcut (forestry) and stand-replacing wildfires to gross AGC_{live} loss. Stand-replacing fires (1.6×10^5 km^2) covering ~60% of the forest-loss area contributed 62% ($-0.10^{-0.09}_{-0.11}$ PgC yr^{-1}) of the gross AGC_{live} loss while other

https://doi.org/10.1038/s41561-022-01087-x

stand-replacing processes (for example, clearcutting and massive insect outbreaks) contributed only ~38% ($-0.06^{-0.06}_{-0.07}$ PgC yr^{-1}).

We further investigated the impacts of wildfires on AGC_{live} losses by considering L-VOD pixels (25 km) that are burned by wildfires over the whole of Siberia, thus considering all fires and not only the stand-replacing ones that coincide with forest area loss in ref. [33]. 'Unburned' pixels were defined as those with an annual burned fraction lower than 1% during 2006–2019. The remaining grid cells were defined as partly burned regions (Methods and Supplementary Fig. 7). In those partly burned areas (3.1 × 106 km2) that cover ~78% of the study region, we found a net AGC_{live} change of $-0.06^{-0.06}_{-0.07}$ PgC yr^{-1} mainly over East Siberia ($-0.03^{-0.03}_{-0.03}$ PgC yr^{-1}) and the Far East ($-0.04^{-0.04}_{-0.04}$ PgC yr^{-1}) whereas AGC_{live} changes in unburned pixels were close to zero (Fig. 1c). Over partly burned regions, the dynamics of biomass are enhanced, with gross AGC_{live} losses ($-0.28^{-0.29}_{-0.27}$ PgC yr^{-1}) and gains ($+0.21^{+0.22}_{+0.21}$ PgC yr^{-1}) being four times larger than the net change ($-0.06^{-0.06}_{-0.07}$ PgC yr^{-1}). Overall, gross AGC_{live} losses of partly burned pixels were 2.8 times larger than the loss from stand-replacing fires ($-0.10^{-0.09}_{-0.11}$ PgC yr^{-1}). This result shows that the Landsat forest-loss data do not capture small-scale forest-loss patches burned by fires and/or that the droughts and many ground fires of low intensity lead to AGC_{live} losses even though they do not cause stand replacement [42].

Simultaneous biomass losses and greening trends

We addressed whether greening trends observed by LAI can be linked with carbon uptake over the Siberian forests. For the period 2010–2019, AGC_{live} decreased significantly ($P < 0.01$) (Fig. 1b) while LAI increased, but non-significantly ($P > 0.05$) (Fig. 1d). The difference between these trends occurred mainly in wildfire-affected L-VOD pixels, where the LAI values were relatively constant while AGC_{live} decreased (Fig. 1c,e).

Net AGC_{live} changes showed a low spatial agreement with LAI changes at 25 km resolution: net changes were of the same sign over 54% of the grid cells, but 37% had negative net AGC_{live} changes and positive changes in LAI (Fig. 2b,d). Considering the spatial trends in AGC_{live} stocks and LAI, 48% of the areas with negative AGC_{live} trends (Supplementary Fig. 8b) showed an LAI-derived greening trend (Supplementary Fig. 8d). Specifically, 80% of the areas with a negative AGC_{live} trend and an LAI greening trend matched the fire-disturbed areas (Fig. 2f). These results suggest that in fire-affected areas, LAI recovers more quickly than fire-related C losses.

To illustrate the differences between post-fire AGC_{live} and LAI trajectories, we selected one L-VOD pixel (Fig. 3) that experienced 26% of forest loss during the 2010–2019 period and 53% of burning in 2012 (Fig. 3c). AGC_{live} and LAI both declined sharply in 2012, and AGC_{live} did not recover in subsequent years, in line with the slow recovery of AGC_{live} after fires in boreal forests [43,44], aggravated by the 2015–2017 subsequent drought. As illustrated by 30 m Landsat images, the obvious forest losses in 2016 (Fig. 3e) against a dense forest (Fig. 3d) in 2011 can be observed in the central region of the 25 km grid cell. By contrast, LAI showed a rapid recovery to pre-fire levels in 2018, only six years after the 2012 massive burning event.

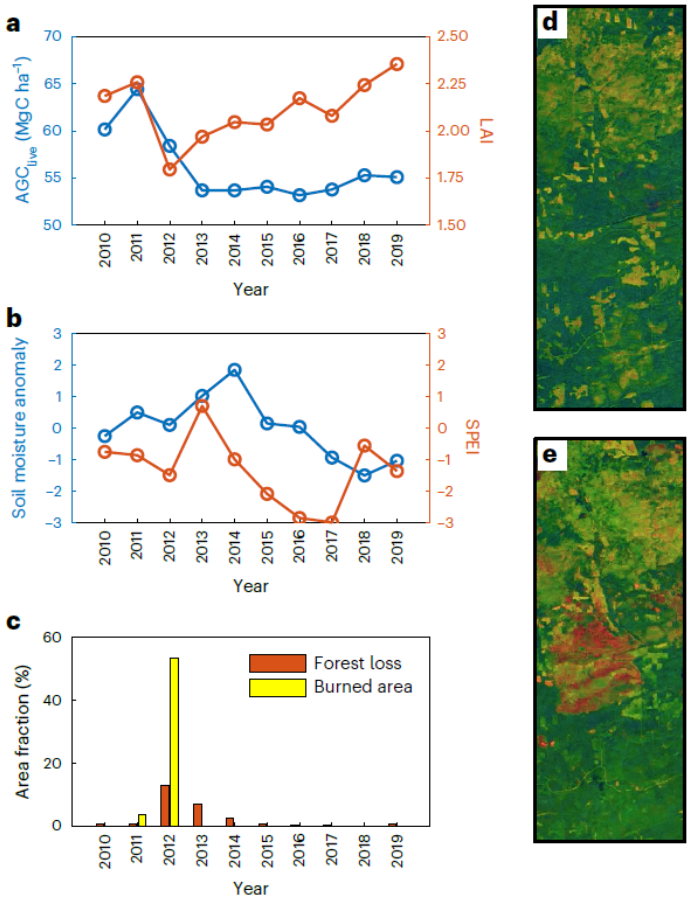

Fig. 3. Interannual variation of AGC_{live}, LAI and hydrological indices for a single 25 km grid cell. **a–c**, AGC_{live} and LAI (**a**), soil moisture anomalies and SPEI (**b**) and forest loss and burn area fraction (**c**) of the 25 km grid cell (central latitude, 58.7° N; longitude, 96.4° W). **d,e**, Landsat/Copernicus images (at a spatial resolution of 30 m) acquired in 2011 (**d**) and 2016 (**e**) within the 25 km grid cell (SMOS pixel).

We then further generalized the study of post-fire AGC_{live} and LAI recovery for a larger area by calculating AGC_{live} and LAI changes across all pixels that burned by more than 10% during the study period and burned only once, to avoid confounding effects of multiple fires (Method). This selection returned 184 pixels covering 0.11 million km^2, related mainly to wildfires in 2012 (31.9%) and 2016 (17.9%), the majority in larch-dominated forests (76.2%) (Supplementary Fig. 9). Both AGC_{live} and LAI decreased after wildfires, and the differences between pre- and post-fire values were significantly correlated with the burned fraction ($P < 0.01$, Fig. 4a), which can also be observed from different tree taxa (for example, pine (Fig. 4b) and larch (Fig. 4c)).

https://doi.org/10.1038/s41561-022-01087-x

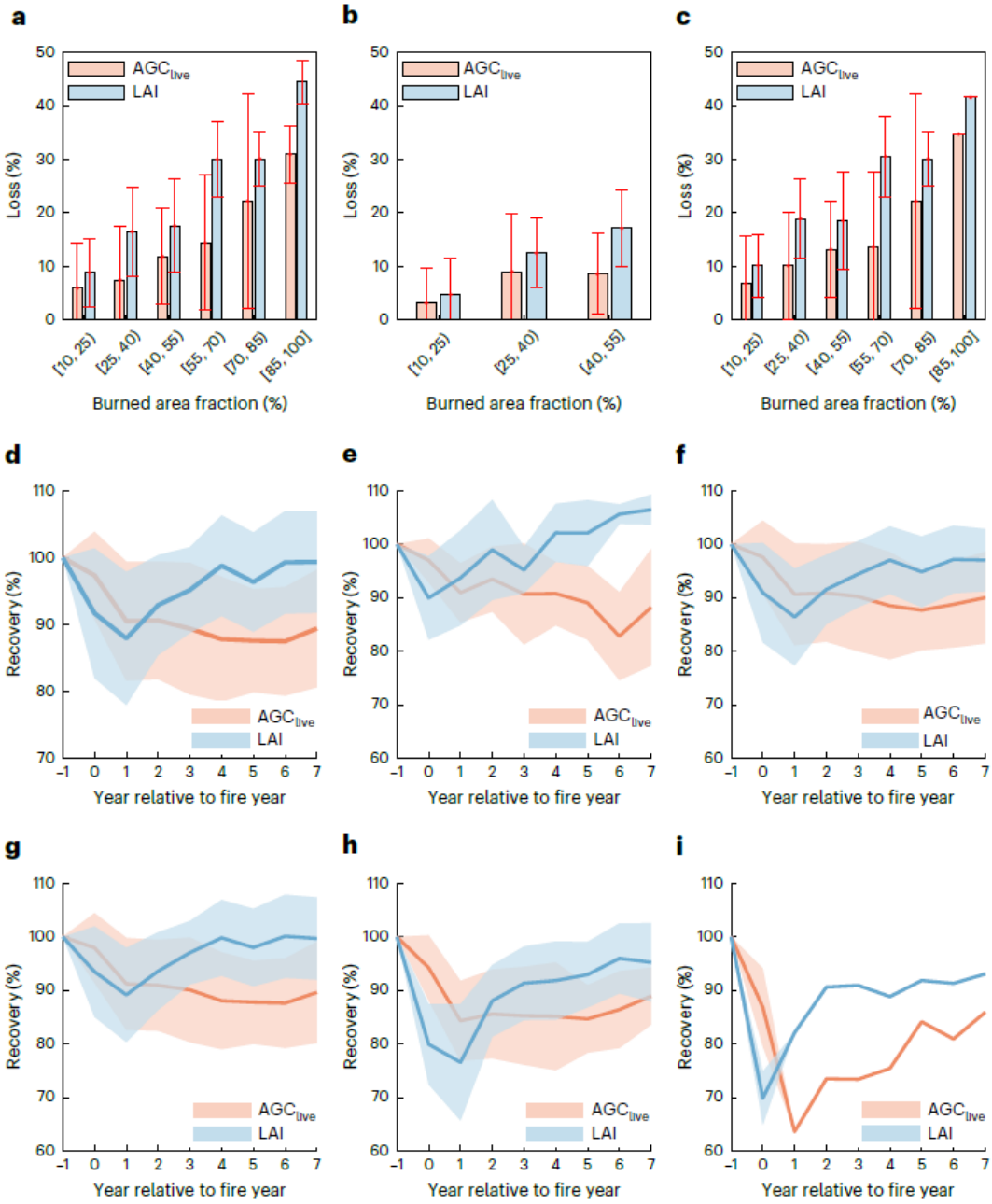

Fig. 4. The responses of AGC_{live} and LAI to wildfire. a–c, The AGC_{live} and LAI losses (%) caused by fire relative to pre-fire AGC_{live} and LAI for the whole of Siberia (n = 184) (**a**), pine (n = 14) (**b**) and larch (n = 144) (**c**). Error bars are one standard deviation from the mean. **d–f**, The AGC_{live} and LAI recoveries (%) for the whole of Siberia (**d**), pine (**e**) and larch (**f**). g–i, Recovery of AGC_{live} and LAI in response to wildfire for the pixels with a burned fraction of 10–40% (n = 154) (**g**), 40–70% (n = 28) (**h**) and >70% (n = 2) (**i**). The centre lines and the shading ranges represent the mean values and one standard deviation, respectively.

Both AGC_{live} and LAI continued to decrease in the first post-fire year (Fig. 4d); thereafter, a quick recovery was observed for LAI while AGC_{live} continued to decrease, reaching its minimum five to six years after the fire event. Seven years after wildfires, LAI had fully recovered to its pre-fire value while AGC_{live} was ~11% below its pre-fire level. Similar evidence was observed from pine (Fig. 4e) and larch forests (Fig. 4f) under a series of burned fractions (Fig. 4g–i). These results show that post-fire AGC_{live} recovery is much slower than LAI recovery, explaining the decoupling of LAI and AGC_{live} trends over Siberian forests during the recent ten years.

https://doi.org/10.1038/s41561-022-01087-x

Implications for boreal carbon balance

Boreal forests of Siberia were estimated to be a carbon sink over the past decades from inventory data analysis and short-wave microwave data, which are prone to saturate with biomass [6,13,37]. Our observations for the recent decade show that the carbon balance of this region is close to neutral. Comparison of our estimates (2010–2019) with the synthesis of forest inventory data (1990–2007) [37] suggests that the relative contribution of live biomass and dead wood to the net C sink has changed in the recent decade. Both live biomass (+0.07 PgC yr^{-1}) and dead wood (+0.10 PgC yr^{-1}) were inferred to be C sinks during 2000–2007 in ref. [37], but our results for 2010–2019 revealed that the live biomass pool decreases (−0.08 PgC yr^{-1}). On the contrary, carbon stocks in CWD made a major contribution to the total C sink (+0.10 PgC yr^{-1}), in line with ref. 37 (+0.10 PgC yr^{-1} for 2000–2007).

We attributed the widespread AGC_{live} losses to drought and wildfire events, supporting previous findings that heatwaves together with wildfire events have affected the AGC balance of Siberian forests [27]. Net negative AGC_{live} changes revealed by L-VOD are confirmed by another high-frequency VOD product (Methods and Supplementary Figs. 10 and 11) and are supported by a recent carbon estimate using optical datasets and high-frequency VOD45 (Supplementary Fig. 12). Our results are also consistent with simulations of vegetation models that projected net changes in AGC_{live} of $-0.05^{-0.05}_{-0.05}$ PgC yr^{-1} for different greenhouse gas emission scenarios between 2000 and 2025 [46]. Note that our estimated carbon sources are larger than those of Xu et al. [45] over the whole study region (−0.08 versus −0.03 PgC yr^{-1} for ref. [45]): West Siberia (+0.01 versus +0.01 PgC yr^{-1} for ref. [45]), East Siberia (−0.03 versus +0.005 PgC yr^{-1}), Far East (−0.05 versus −0.04 PgC yr^{-1}). This difference was observed mainly over the fire-disturbed regions of East Siberia, where Xu et al. [45] found a carbon sink in contrast to our results of carbon losses. This could be attributed partly to the fact that the optical data used in the estimates of Xu et al. [45] could not detect the carbon losses over fire-disturbed regions, supported by our results showing that no simple relationship exists between greening as measured from optical vegetation indices and changes in AGC_{live}.

Boreal greening expresses an increase in vegetation productivity and an associated gross land carbon uptake as inferred from satellite records [6,8] and forest inventories [37]. Our results highlight the lagged recovery of AGC_{live} compared with photosynthetic activity [47,48] in Siberian forests due to their different responses to wildfire events, implying that AGC_{live} losses induced by wildfire events can be synchronous with post-fire greening. This complex recovery pathway of Siberian forests exemplifies that caution should be taken when interpreting greening trends as carbon sinks without the use of in situ data to corroborate conclusions.

Our estimates of gross loss of AGC_{live} ($-0.16^{-0.14}_{-0.18}$ PgC yr^{-1}) resulting from forest loss for 2010–2019 are higher than the 20 yr (2000–2019) average gross loss of −0.09 PgC yr^{-1} reported by Harris et al. [49], suggesting that the flux from gross forest loss increased in the recent ten years. This can be attributed mainly to the 111% increase of forest loss in 2010–2019 (2.7×10^5 km^2) compared with 2000–2009 (1.3×10^5 km^2) as detected by the dataset of Hansen et al. [33], albeit with some caution when comparing the forest-loss dataset of ref. [33] between different periods. For the 2010 decade, we estimated a live gross carbon loss four times higher than that estimated by Harris et al. [49] over 2000–2019 ($-0.37^{-0.36}_{-0.39}$ PgC yr^{-1} versus −0.09 PgC yr^{-1}). The estimates of Harris et al. [49] do not distinguish areas of complete canopy removal from partial disturbances and may thus neglect the degradation-induced carbon losses (for example, from selective logging, mortality associated with droughts, insect outbreaks or understory fires). Similarly, gross AGC_{live} gains as estimated by L-VOD for the 2010 decade were higher than those estimated by Harris et al. [49] ($+0.29^{+0.31}_{+0.29}$ PgC yr^{-1} versus +0.24 PgC yr^{-1}). Harris et al. [49] reported forest gains only as transition probabilities from non-forest to forest across the period. Notably, AGC_{live} gains reported by Harris et al. [49] do not include the post-disturbance AGC_{live} recovery and AGC_{live} gains resulting from vegetation dynamics (for example, the encroachment of trees and shrubs into grasslands or increases in tree density in undisturbed forests).

Considering that full AGC_{live} recovery during post-disturbance succession may require several decades as found at site scale [50], at a regional scale [51] and at a continental scale from our results,

attention should be paid to preventing disturbances and enhancing the potential for boreal forest restoration and reforestation. Implementing timely management strategies with a strong focus on preventing natural disturbance and enhancing forest resilience is thus pivotal as a means to preserve the boreal regions as a durable carbon sink.

Methods

Siberian forest regions

Our study region was located in the Siberian forest regions, consisting of West Siberia (49.67°–66.14° N, 59.38°–89.82° E), East Siberia (49.08°–67.12° N, 79.09°–121.82° E) and Far East (43.13°–69.66° N, 105.74°–179.89° E) regions (the three geographic regions refer to ref. [52]). To identify tree cover and canopy height, we used the MOD44B v.6 Vegetation Continuous Fields yearly product in 2010 [53] and the Geoscience Laser Altimeter System forest canopy height product in 2005 [54], respectively, which were aggregated to 25 km spatial resolution to match the spatial resolution of the Soil Moisture and Ocean Salinity (SMOS) data by averaging pixels. To identify land cover, we also used the 500 m moderate-resolution imaging spectroradiometer (MODIS) land-cover map provided by Broxton et al. [55], which was aggregated to 25 km resolution by dominant class within each 25 km grid cell. 'Dominant' refers to the class that has the largest number of 500 m native-resolution pixels within each 25 km grid cell. The forest regions (Fig. 1a) were defined as tree cover > 15% and canopy height > 5 m using the aggregated 25 km Vegetation Continuous Fields and forest canopy height products, respectively. We masked non-forest SMOS pixels dominated by 'closed shrublands', 'open shrublands', 'woody savannahs', 'savannahs', 'urban and built-up', 'snow and ice', 'water', 'grasslands' and 'barren or sparsely vegetated' using the aggregated 25 km MODIS land-cover map. Pixels dominated by the 'wetland' land cover were also masked as L-VOD is underestimated when the observation footprint contains substantial open water bodies. Further, accounting for the availability of AGC_{live} derived from L-VOD, our study area in Siberia covers ~4.0×10^6 km^2 (Fig. 1a). Our analysis focused on AGC_{live} and CWD and did not assess changes in other carbon stocks (for example, litter or soil organic matter).

Benchmark maps of AGClive density

Fan et al. [32] used four pantropical static AGC_{live} benchmark maps for calibrating the L-VOD/AGC_{live} relationship. In this Article, we used three of the most recent global static AGC_{live} benchmark maps (Supplementary Fig. 13a–c) to calibrate L-VOD (Supplementary Fig. 13d), including the global maps provided by Saatchi et al. [56], http://cci.esa.int/biomass and Santoro et al. [57], hereafter referred to as the 'Saatchi', 'CCI' and 'GlobBiomass' maps, respectively. The Saatchi map used in the present study is an updated version that represents AGC_{live} circa 2015 [58]. The CCI and GlobBiomass maps used in the present study correspond to the years 2017 and 2010, respectively. The original units of above-ground biomass density (Mg ha^{-1}) were converted to AGC_{live} density (MgC ha^{-1}) by multiplying the original values by a factor of 0.5 (ref. [59]). All AGC_{live} maps were aggregated to 25 km spatial resolution to match the spatial resolution of the SMOS data by averaging AGC_{live} pixels within the SMOS grid cells.

SMOS-IC soil moisture and L-VOD

Several studies have combined datasets from both forest inventory plots and remote sensing to generate spatial maps of forest above-ground biomass estimates at multi-year

time frames [56,60,61] based on canopy height estimates from the Geoscience Laser Altimeter System lidar (light detection and ranging) sampling strips and vegetation indices from optical images (MODIS). However, these global maps are generally static (available for one or a few years only). The recently developed L-VOD AGC_{live} dataset is one of the major satellite-based data sources for adding a temporal dynamic to these maps that allows monitoring interannual changes of AGC_{live} at the global scale.

The L-VOD AGC_{live} data were derived using the L-VOD product, which is developed using the SMOS-IC algorithm in version 2 [62,63] designed by INRAE (Institut National de la Recherche Agronomique) on the basis of the SMOS satellite images. As in ref. [32], the root mean square error (RMSE) between the measured and simulated brightness temperatures (referred to as RMSE-TB) associated with the SMOS-IC product was used to filter out observations affected by radio frequency interference, which perturbs the natural microwave emission from Earth's surface measured by passive microwave systems. We excluded daily observations, influenced by radio frequency interference effects, for which RMSE-TB was larger than 6 K. Monthly L-VOD and soil moisture from June to September were produced as the medians of all high-quality ascending and descending L-VOD retrievals with more than four valid observations per month. Robust estimates of annual L-VOD and soil moisture were then obtained as the averages of the monthly products (June–September); pixels that have at least one missing month within one year (June–September) were filtered out in this study. The annual changes in precipitation and SMOS soil moisture are quite consistent over the West Siberia, East Siberia and Far East regions (Supplementary Fig. 2), adding confidence in the quality of the simultaneous retrievals of SM and L-VOD from the SMOS observations over Siberia.

L-VOD-retrieved AGC_{live}

The method used here to compute annual AGC_{live} from yearly L-VOD is the same as the one used in ref. [32], where it is described in detail. AGC_{live} was computed from L-VOD on the basis of an empirical calibration function (equation (1)) using gridded reference AGC_{live} datasets:

$$AGC_{live} = a \times VOD^{b} \quad (1)$$

where a and b are two best-fit parameters (Supplementary Table 1) and VOD is the yearly L-VOD data. As in ref. [32], we used the year 2011 for calibrating equation (1) (the year used for calibration proved to have very little impact on the calibrated curves). An illustration of the calibrated relationships between L-VOD and AGC_{live} based on the GlobBiomass, Saatchi and CCI maps is given in Supplementary Fig. 14. We converted the yearly L-VOD map into maps of yearly AGC_{live} density (MgC ha^{-1}) for 2010–2019 using equation (1). Regional AGC_{live} stocks were obtained by multiplying the L-VOD-derived AGC_{live} density by the area of the corresponding L-VOD pixels.

The AGC_{live} benchmark maps contain uncertainties and biases, and no single map can be considered fully reliable [64,65]. The L-VOD map matched different benchmark maps of above-ground living carbon in the study region (Supplementary Fig. 14). We used all the different maps to fit equation (1) for the global scale and for Siberia separately (Supplementary Fig. 14). Six calibrations of equation (1) were thereby obtained (Supplementary Table 1). Note that the calibrated relationships between L-VOD and the benchmark maps were consistent both at the global scale and for Siberia alone (Supplementary Fig. 14), showing that the statistical relationship between L-VOD and vegetation carbon stocks is robust over different regions of interest. Moreover, the general

relationship between the reference map and the annual L-VOD map was stable between individual years. In addition, the net AGC_{live} changes from 2010 to 2019 estimated by the relationship calibrated on the basis of the live AGC benchmark maps and annual L-VOD were very similar between individual years (Supplementary Fig. 15).

We used all the six calibrations to create six maps of AGC_{live} stocks. We used the median of these six maps to calculate yearly AG AGC_{live} Clive maps during 2010–2019. The minima and maxima were also reported as they provide estimates of the uncertainty associated with the retrieved AGC_{live} estimates used in this study and that relates to systematic errors in the reference biomass maps [32].

Fan et al. [32] have done an extensive analysis of the uncertainties associated with AGC_{live} and AGC_{live} changes, including (1) internal uncertainties associated with the L-VOD derived AGC_{live} estimates and (2) external uncertainties associated with the errors in the reference biomass maps used to calibrate L-VOD from equation (1). Fan et al. [32] showed that external uncertainties were strongly dominant over the internal uncertainties and that combining both of them, the total relative uncertainties associated with AGC_{live} and the AGC_{live} changes are on the order of 20–30%.

At large scale (global and Siberia regions), the cross-validation results showed high correlation (r) values and low RMSE values in the AGC_{live} estimates by comparing the six AGC_{live} estimates with the respective reference maps (Supplementary Table 2). This suggests that there is no obvious regional bias between the reference datasets and the AGC_{live} estimates for the three continents. Moreover, the 95% bootstrap confidence interval of the AGC_{tot} estimates retrieved using each set of calibrated parameters is small, indicating that the internal uncertainties caused by sampling errors are small (Supplementary Table 2).

AGC_{tot}

Here, ignoring soil, branch and fine litter changes, AGC_{tot} is defined as the sum of AGClive estimated by L-VOD and dead AGC (for example, total CWDC ($CWDC_{tot}$)), accounting for the net change of live and dead AGC in terrestrial ecosystems at temporal and spatial scales:

$$AGC_{tot} = AGC_{live} + CWDC_{tot} \quad (2)$$

Over Siberian forests, CWDCtot is driven mainly by the background mortality and forest disturbances (for example, wildfire, wind storm and drought). The carbon loss from CWDCtot was determined using decomposition and consumption by fires [14]. This decomposition rate is low because of the low temperature and short growing season [66] relative to tropical forests. Stand-replacing fire is the main cause of natural tree die-off in Siberia [16,67], increasing the carbon stock of CWD (including dead standing and fallen trees) but meanwhile consuming CWDC. More specifically, the carbon loss from $CWDC_{tot}$ was assumed to be induced by decomposition and combustion by stand-replacing fire. Here, the $CWDC_{tot}$ fuels were from (1) mortality of trees caused by stand-replacing fire ($CWD_{stand\text{-}replacing}$), (2) the initial accumulation for years before 2010 ($CWD_{initial}$) and (3) the mortality of trees caused by annual background mortality ($CWD_{backgroundmortality}$).

Thus, CWDCtot was calculated as:

$$CWDC_{tot} = CWD_{stand-replacing} + CWD_{initial} + CWD_{backgroundmortality} \quad (3)$$

The detailed calculation of $CWDC_{tot}$ is given in Supplementary Text.

https://doi.org/10.1038/s41561-022-01087-x

Vegetation and climate variables

Annual burned fraction. The MOD14A2 active fire product (MODIS/Terra Thermal Anomalies and Fire 8-Day L3 Global 1 km v.006) is an eight-day composite containing the maximum value of the individual pixel classes that are in each 1 km grid cell over the eight-day period [34] (the newer 6.1 version is available from https://lpdaac.usgs.gov/products/mod14a2v006/). Each MOD14A2 file consists of two layers (a fire mask and associated quality information). We first identified the good-quality observations (nominal and high confidence) of MOD14A2 active fire, then we generated annual active fire maps including all pixels where active fire occurred in a year (each 1 km pixel was assumed to be completely burned) during 2010–2019. Annual burned fraction was calculated at the resolution of SMOS as the proportion of the summed areas of active fire (assuming that each 1 km pixel was completely burned) within each 25 km grid cell.

MODIS LAI product. We used the MODIS LAI product (the MCD15A2H, v.6, level 4), which is an eight-day composite dataset with 500 m pixel size [68]. High-quality LAI data from June to September during 2010–2019 were aggregated to an annual composite at 25 km spatial resolution by averaging from their original resolution to match the SMOS grid.

Forest loss. We used the 'yearloss' forest area loss map33 to calculate forest-loss rates. Forest loss was defined as a stand-replacement disturbance or a change from a forest to a non-forest state. Each 30 m pixel in the yearloss Landsat data was labelled with a loss year representing the loss of forest (defined as tree higher than 5 m) cover detected primarily during 2000–2019. Here, forest percentage loss rates during the study period 2010–2019 were calculated at the resolution of SMOS grid as the proportion of the summed areas of forest loss (detected by the yearloss map) within each SMOS grid cell (~25 km). Note that forest-loss product [33] represents temporal or permanent loss of tree cover after disturbances (wildfire or clearcutting).

Stand-replacing wildfires product. This product from van Wees et al. [69] estimates areas where forest loss overlaps with fire detection (burn area or active fires) at a spatial resolution of 500 m. Its definition of wildfire-related forest loss includes any sequence between fire and forest loss, including simultaneous occurrence of fire and forest loss (for example, wildfire), fire followed by forest loss (for example, tree mortality after fire damage) and forest loss followed by fire (for example, burning of slash after felling, which mostly happens in the same year as the felling). Here, annual stand-replacing fire fraction was calculated at the resolution of SMOS as the proportion of the summed areas of stand-replacing fire within each SMOS grid cell (~25 km).

SPEI-12. SPEI-12 refers to the droughts at a 12-month timescale, provided from the global SPEI database (https://spei.csic.es/) [70]. SPEI is amulti-scalar index frequently used to quantify drought and is based on a climate–water balance. As opposed to some existing indices of climatological drought, SPEI incorporates multiple climatological factors, including precipitation and temperature, which is imperative for assessing the influence of climate change on drought.

Tree species map. Tree species map [71] has a spatial resolution of 200 m. The product was aggregated to 25 km resolution by dominant species within each SMOS grid cell. The dominant species is the species that has the largest number of 200 m native-resolution pixels within each SMOS grid cell. The tree species over the study region included pine (14%), spruce (2%), fir (2%), larch (63%), juniper (6%), oak (1%), birch (11%) and maple (1%). In addition, the tree species used for the calculation of AGC_{live}/LAI recovery are birch, maple, larch, spruce and pine (Supplementary Fig. 9).

VOD_{LPDR}. VOD_{LPDR} at a high-frequency band (X-band) is provided by the global land parameter data record (LPDR) [72], which is sensitive to the canopy biomass water content and saturates in densely vegetated areas faster than low-frequency L-VOD but much less than optical indices [73]. High-quality VOD_{LPDR} from June to September during 2010–2019 was used to calculate the yearly VOD_{LPDR}.

Greening trend was evaluated on the basis of the Theil–Sen test, which is used to determine the trend direction, while the Mann–Kendall test was used to assess the statistical significance of the trends, regarding trends as significant when $P < 0.05$.

Net gains/losses in AGC. Net changes in AGC were calculated as the difference in AGC between two years. For example, net changes in AGC during 2010–2019 were calculated as the AGC in 2019 minus that in 2010. A positive net AGC change indicates net gain (sink) in AGC, while a negative net AGC change indicates net carbon losses (source).

Gross changes in AGC_{live} were calculated by cumulating positive/negative changes in AGC_{live} for consecutive years from 2010 to 2019, respectively.

Gross AGC_{live} loss caused by forest loss and forest degradation. The gross AGC_{live} loss (Gross AGC loss) in a grid cell is controlled by forest area loss (Gross AGC $loss_{forest\ loss}$), forest degradation (Gross AGC $loss_{degradation}$) and other mechanisms (Gross AGC $loss_{others}$) such as non-forest biomass decreases (equation (4)). We conducted a simple estimate of forest loss versus degradation within each SMOS grid cell using the method proposed by Harris et al. [40] and Qin et al. [41]. First we calculated the gross AGC_{live} loss in each 25 km grid cell. Second, we multiplied the gross forest area loss (calculated using Hansen et al. [33]) during 2011–2019 by the AGC_{live} density in 2010 to estimate separately the contribution from forest loss to gross AGC_{live} loss (equation (5)). The difference between gross AGC_{live} loss and this forest loss (Gross AGC $loss_{forest\ loss}$) contribution is attributed to degradation (equation (6))

$$Gross\ AGC\ loss_{forest\ loss} \cong \sum(Gross\ forest\ area\ loss) \times AGC_{density} \quad (5)$$

$$Gross\ AGC\ loss_{degradation} \cong\ Gross\ AGC\ loss - Gross\ AGC\ loss_{forest\ loss} \quad (6)$$

The gross AGC_{live} loss by forest area loss (Gross AGC $loss_{forest\ loss}$) was further separated into contributions of stand-replacing wildfires (Gross AGC $loss_{stand\text{-}replacing\ fire}$) and other factors (for example, clearcutting and severe drought that suppress forests) to AGC_{live} losses. Stand-replacing fire areas during the study period 2011–2019 were calculated as the proportion of the areas of stand-replacing fire within each SMOS grid cell (~25 km). Second, we multiplied the AGC_{live} loss from stand-replacing fires leading to forest loss:

$$Gross\ AGC\ loss_{stand} - replacing\ fire \cong \sum(Gross\ areas_{stand-replacing\ fire}) \times AGC_{density} \quad (7)$$

Losses of AGC_{live} and LAI resulting from the immediate effect of fire in selected pixels. Wildfire-related losses of AGC_{live} and LAI were investigated over selected burned pixels. Fire recurrence affects community development and landscape diversity. Post-wildfire dynamics depend on the interval of wildfire recurrence, and forests affected by recurrent wildfires in a short period will have a different behaviour from those affected by a single wildfire [74]. In this study, we focused on selected burned pixels that were burned only once. Selected pixels were determined from two conditions: (1) burned only once during 2010–2019 with the burned area fraction larger than 10% in the fire year and (2) burned area fraction less than 1% in the unburned years during 2006–2019 using the MOD14A2 product.

Taking AGC_{live} as an example, forest AGC_{live} losses (%) were calculated by the maximum pre- and post-fire AGC_{live} difference (year before fire minus fire year or fire year plus 1), relative to pre-fire AGC_{live} (see equation (8)). The timing of the fire influenced which year was selected: fires early in the season had the largest impact in the year of the fire, whereas late-season fires had the largest impact during the following year. One hundred eighty-four pixels were selected following the defined selection criteria as:

$$AGC_{loss}\ (\%) = \frac{max(AGC_{prefire} - AGC_{fire},\ AGC_{prefire} - AGC_{fire+1})}{AGC_{prefire}} \quad (8)$$

where AGC_{loss} is the live AGC losses resulting from the immediate effect of fire. $AGC_{prefire}$, AGC_{fire} and AGC_{fire+1} are the AGC_{live} stocks in the one year before wildfire, the wildfire year and the one year after wildfire, respectively. LAI forest losses were also computed from equation (8) by substituting 'AGC' with 'LAI'.

AGC_{live} and LAI recovery in the post-wildfire period. Post-fire AGC_{live} and LAI recovery in the Siberian forests were studied by analysing the selected burned pixels. The AGC_{live} time series of these selected pixels were first shifted to align the fire years of all fires considered (Supplementary Fig. 16).

'Relative year zero' is the fire year, negative values are pre-fire years (for example, '−1' year means one year before fire) and positive values are post-fire years (for example, '2' year means the second year after fire). Then, at the *i*th year after fire, the recovery ratio ($Recovery_i$ (%)) is calculated from pre-fire live AGC (AGC_{-1}) and live AGC at *i*th year in the post-fire period (AGC_i) using equation (9). Thus, the recovery ratio for each year was plotted in Fig. 4 in the main text as the AGC_{live} recovery trajectory. Forest recovery trajectory was also estimated from LAI following the same method.

$$Recovery_i = \frac{AGC_i}{AGC_{-1}} \times 100\%, -1 \le i \le 9 \quad (9)$$

Uncertainties associated with the vegetation indices The pixels with a burned fraction larger than 10% were selected to calculate the AGC_{live}/LAI response to wildfire events. Although our results suggested that wildfire is the main reason for the divergent response between AGC_{live} and LAI during 2010–2019, the heatwave events that cause wildfires in the Siberian ecosystem also cause degradations due to water stress and mortality. So the AGC_{live}/LAI changes that we computed within the selected pixels could be attributed to both climate (drought and heatwave) and fires. It is difficult to identify and separate the relative contributions of climate and fire in the AGC_{live}/LAI changes due to the coarse spatial resolution (~25 km) of the L-VOD-derived AGC_{live}. Similarly, due to this coarse spatial resolution, we failed to separate pixel-scale carbon gains and losses due to deforestation, regeneration, livestock pressure, conservation, fires and other events [73]. A detailed description of the uncertainties associated with the AGC_{live} product was summarized in ref. [32].

LAI uncertainties include the limitations of data availability caused by the low temporal sampling frequency (a few days to a few weeks) of the MODIS data, which also introduces temporal scale-dependent effects that may be magnified in Arctic systems.

For example, if, due to cloud or aerosol effects, most MODIS observations over one pixel are available in June for year Y and in September for year Y + 1, it is difficult to interpret the changes in LAI between years Y and Y + 1. Are these changes due to greening or disturbances or to natural phenological effects? In addition, the greening/browning trends of LAI can vary owing to a suite of intrinsic (for example, sensor design or quality flagging algorithms), extrinsic (for example, atmospheric conditions, sun angle or snow cover) and biological factors [28].

Data availability

L-VOD and soil moisture data from this study are freely available from the SMOS-IC website (https://ib.remote-sensing.inrae.fr/). AGCtot, AGClive and CWDC products are freely available from https://doi.org/10.11888/Terre.tpdc.272842. The Saatchi biomass map is available upon request from Dr. S. Saatchi (sasan.s.saatchi@jpl.nasa.gov). Tree species maps are available upon request from D. Schepaschenko (schepd@iiasa.ac.at) or from http://webarchive.iiasa.ac.at/Research/FOR/forest_cdrom/english/for_prod_en.html. Additional data used in the paper are publicly available, with their locations provided in the respective references.

Online content

Any methods, additional references, Nature Portfolio reporting summaries, source data, extended data, supplementary information, acknowledgements, peer review information; details of author contributions and competing interests; and statements of data and code availability are available at https://doi.org/10.1038/s41561-022-01087-x.

References

1. Keenan, R. J. et al. Dynamics of global forest area: results from the FAO Global Forest Resources Assessment 2015. For. Ecol. Manage. 352, 9–20 (2015).
2. Arneth, A. et al. in Special Report on Climate Change and Land (eds Shukla, P. R. et al.) Ch. 1 (IPCC, 2019).
3. Piao, S. et al. Growing season extension and its impact on terrestrial carbon cycle in the Northern Hemisphere over the past 2 decades. Glob. Biogeochem. Cycles 21, GB3018 (2007).
4. Chen, C. et al. China and India lead in greening of the world through land-use management. Nat. Sustain. 2, 122–129 (2019).
5. Piao, S. et al. Characteristics, drivers and feedbacks of global greening. Nat. Rev. Earth Environ. 1, 14–27 (2020).
6. Liu, Y. Y. et al. Recent reversal in loss of global terrestrial biomass. Nat. Clim. Change 5, 470–474 (2015).
7. Chen, J. M. et al. Vegetation structural change since 1981 significantly enhanced the terrestrial carbon sink. Nat. Commun. 10, 4259 (2019).
8. Myneni, R. B. et al. Increased plant growth in the northern high latitudes from 1981 to 1991. Nature 386, 698–702 (1997).
9. Filipchuk, A. et al. Russian forests: a new approach to the assessment of carbon stocks and sequestration capacity. Environ. Dev. 26, 68–75 (2018).
10. Goodale, C. L. et al. Forest carbon sinks in the Northern Hemisphere. Ecol. Appl. 12, 891–899 (2002).
11. Tchebakova, N. M. et al. Energy and mass exchange and the productivity of main Siberian ecosystems (from eddy covariance measurements). 2. Carbon exchange and productivity. Biol. Bull. 42, 579–588 (2015).
12. Vaganov, E. A. et al. Forests and swamps of Siberia in the global carbon cycle. Contemp. Probl. Ecol. 1, 168–182 (2008).
13. Schepaschenko, D. et al. Russian forest sequesters substantially more carbon than previously reported. Sci. Rep. 11, 12825 (2021).
14. Shvidenko, A. & Schepaschenko, D. Climate change and wildfires in Russia. Contemp. Probl. Ecol. 6, 683–692 (2013).
15. Bradshaw, C. J. A. & Warkentin, I. G. Global estimates of boreal forest carbon stocks and flux. Glob. Planet. Change 128, 24–30 (2015).
16. Curtis, P. G. et al. Classifying drivers of global forest loss. Science 361, 1108–1111 (2018).
17. Sukhinin, A. I. et al. AVHRR-based mapping of fires in Russia: new products for fire management and carbon cycle studies. Remote Sens. Environ. 93, 546–564 (2004).
18. Soja, A. J. et al. Climate-induced boreal forest change: predictions versus current observations. Glob. Planet. Change 56, 274–296 (2007).
19. Dolman, A. J. et al. An estimate of the terrestrial carbon budget of Russia using inventory-based, eddy covariance and inversion methods. Biogeosciences 9, 5323–5340 (2012).
20. Schaphoff, S. et al. Tamm review: Observed and projected climate change impacts on Russia's forests and its carbon balance. For. Ecol. Manage. 361, 432–444 (2016).
21. de Jong, R. et al. Trend changes in global greening and browning: contribution of short-term trends to longer-term change. Glob. Change Biol. 18, 642–655 (2012).
22. Buermann, W. et al. Recent shift in Eurasian boreal forest greening response may be associated with warmer and drier summers. Geophys. Res. Lett. 41, 1995–2002 (2014).
23. Rödig, E. et al. Spatial heterogeneity of biomass and forest structure of the Amazon rain forest: Linking remote sensing, forest modelling and field inventory. Glob. Ecol. Biogeogr. 26, 1292–1302 (2017).
24. Quegan, S. et al. Estimating the carbon balance of central Siberia using a landscape-ecosystem approach, atmospheric inversion and dynamic global vegetation models. Glob. Change Biol. 17, 351–365 (2011).
25. Gurney, K. R. et al. Interannual variations in continental-scale net carbon exchange and sensitivity to observing networks estimated from atmospheric CO2 inversions for the period 1980 to 2005. Glob. Biogeochem. Cycles 22, GB3025 (2008).

26. Stephens, B. B. et al. Weak northern and strong tropical land carbon uptake from vertical profiles of atmospheric CO2. Science 316, 1732–1735 (2007).
27. Leskinen, P. et al. Russian Forests and Climate Change: What Science Can Tell Us 11 (EFI, 2020); https://doi.org/10.36333/wsctu11.
28. Myers-Smith, I. H. et al. Complexity revealed in the greening of the Arctic. Nat. Clim. Change 10, 106–117 (2020).
29. Stow, D. A. et al. Remote sensing of vegetation and land-cover change in Arctic tundra ecosystems. Remote Sens. Environ. 89, 281–308 (2004).
30. Karlsen, S. R. et al. A new NDVI measure that overcomes data sparsity in cloud-covered regions predicts annual variation in ground-based estimates of high Arctic plant productivity. Environ. Res. Lett. 13, 025011 (2018).
31. Ding, Z. et al. Nearly half of global vegetated area experienced inconsistent vegetation growth in terms of greenness, cover, and productivity. Earths Future 8, e2020EF001618 (2020).
32. Fan, L. et al. Satellite-observed pantropical carbon dynamics. Nat. Plants 5, 944–951 (2019). Nature Geoscience Article https://doi.org/10.1038/s41561-022-01087-x
33. Hansen, M. C. et al. High-resolution global maps of 21st-century forest cover change. Science 342, 850–853 (2013).
34. Giglio, L. et al. The collection 6 MODIS active fire detection algorithm and fire products. Remote Sens. Environ. 178, 31–41 (2016).
35. Blunden, J. & Arndt, D. S. State of the climate in 2015. Bull. Am. Meteorol. Soc. 97, Si–S275 (2016).
36. Bastos, A. et al. Was the extreme Northern Hemisphere greening in 2015 predictable? Environ. Res. Lett. 12, 044016 (2017).
37. Pan, Y. et al. A large and persistent carbon sink in the world's forests. Science 333, 988–993 (2011).
38. Kukavskaya, E. A. et al. Biomass dynamics of central Siberian Scots pine forests following surface fires of varying severity. Int. J. Wildland Fire 23, 872–886 (2014).
39. Gauthier, S. et al. Boreal forest health and global change. Science 349, 819 (2015).
40. Harris, N. L. et al. Baseline map of carbon emissions from deforestation in tropical regions. Science 336, 1573 (2012).
41. Qin, Y. et al. Carbon loss from forest degradation exceeds that from deforestation in the Brazilian Amazon. Nat. Clim. Change 11, 442–448 (2021).
42. Rogers, B. M. et al. Influence of tree species on continental differences in boreal fires and climate feedbacks. Nat. Geosci. 8, 228–234 (2015).
43. Shvetsov, E. G. et al. Assessment of post-fire vegetation recovery in southern Siberia using remote sensing observations. Environ. Res. Lett. 14, 055001 (2019).
44. Wang, J. A. et al. Disturbance suppresses the aboveground carbon sink in North American boreal forests. Nat. Clim. Change 11, 435–441 (2021).
45. Xu, L. et al. Changes in global terrestrial live biomass over the 21st century. Sci. Adv. 7, eabe9829 (2021).
46. Shuman, J. K. et al. Forest forecasting with vegetation models across Russia. Can. J. For. Res. 45, 175–184 (2014).
47. Flannigan, M. et al. Impacts of climate change on fire activity and fire management in the circumboreal forest. Glob. Change Biol. 15, 549–560 (2009).
48. Yuan, W. et al. Differentiating moss from higher plants is critical in studying the carbon cycle of the boreal biome. Nat. Commun. 5, 4270 (2014).
49. Harris, N. L. et al. Global maps of twenty-first century forest carbon fluxes. Nat. Clim. Change 11, 234–240 (2021).
50. Larjavaara, M. et al. Post-fire carbon and nitrogen accumulation and succession in Central Siberia. Sci. Rep. 7, 12776 (2017).
51. Berner, L. T. et al. Cajander larch (Larix cajanderi) biomass distribution, fire regime and post-fire recovery in northeastern Siberia. Biogeosciences 9, 3943–3959 (2012).
52. Houghton, R. A. et al. Mapping Russian forest biomass with data from satellites and forest inventories. Environ. Res. Lett. 2, 045032 (2007).

53. DiMiceli, C. et al. Annual Global Automated MODIS Vegetation Continuous Fields (MOD44B) at 250 m Spatial Resolution for Data Years Beginning Day 65, 2000–2014, Collection 5 Percent Tree Cover v.6 (Univ. Maryland, 2017).
54. Simard, M. et al. Mapping forest canopy height globally with spaceborne lidar. J. Geophys. Res. 116, G04021 (2011).
55. Broxton, P. et al. A global land cover climatology using MODIS data. J. Appl. Meteorol. Climatol. 53, 1593–1605 (2014).
56. Saatchi, S. S. et al. Benchmark map of forest carbon stocks in tropical regions across three continents. Proc. Natl Acad. Sci. USA 108, 9899–9904 (2011).
57. Santoro, M. et al. The global forest above-ground biomass pool for 2010 estimated from high-resolution satellite observations. Earth Syst. Sci. Data. 13, 3927–3950 (2021).
58. Carreiras, J. M. B. et al. Coverage of high biomass forests by the ESA BIOMASS mission under defense restrictions. Remote Sens. Environ. 196, 154–162 (2017).
59. Penman, J. et al. Good Practice Guidance for Land Use, Land-Use Change and Forestry (IGES, 2013).
60. Avitabile, V. et al. An integrated pan-tropical biomass map using multiple reference datasets. Glob. Change Biol. 22, 1406–1420 (2016).
61. Baccini, A. et al. Estimated carbon dioxide emissions from tropical deforestation improved by carbon-density maps. Nat. Clim. Change 2, 182–185 (2012).
62. Fernandez-Moran, R. et al. SMOS-IC: an alternative SMOS soil moisture and vegetation optical depth product. Remote Sens. 9, 457 (2017).
63. Wigneron, J.-P. et al. SMOS-IC data record of soil moisture and L-VOD: historical development, applications and perspectives. Remote Sens. Environ. 254, 112238 (2021).
64. Mitchard, E. T. A. et al. Markedly divergent estimates of Amazon forest carbon density from ground plots and satellites. Glob. Ecol. Biogeogr. 23, 935–946 (2014).
65. Mitchard, E. T. A. et al. Uncertainty in the spatial distribution of tropical forest biomass: a comparison of pan-tropical maps. Carbon Balance Manage. 8, 10 (2013).
66. Harmon, M. E. et al. Release of coarse woody detritus-related carbon: a synthesis across forest biomes. Carbon Balance Manage. 15, 1 (2020).
67. Bartalev, S. A. & Stytsenko, F. V. Assessment of forest-stand destruction by fires based on remote-sensing data on the seasonal distribution of burned areas. Contemp. Probl. Ecol. 14, 711–716 (2021).
68. Myneni, R. et al. MOD15A2H MODIS/Terra Leaf Area Index/FPAR 8-Day L4 Global 500 m SIN Grid v.006 (LAADS DAAC, 2015).
69. van Wees, D. et al. The role of fire in global forest loss dynamics. Glob. Change Biol. 27, 2377–2391 (2021).
70. Vicente-Serrano, S. M. et al. A multiscalar drought index sensitive to global warming: the Standardized Precipitation Evapotranspiration Index. J. Clim. 23, 1696–1718 (2010).
71. Schepaschenko, D. et al. A new hybrid land cover dataset for Russia: a methodology for integrating statistics, remote sensing and in situ information. J. Land Use Sci. 6, 245–259 (2011).
72. Du, J. et al. A global satellite environmental data record derived from AMSR-E and AMSR2 microwave Earth observations. Earth Syst. Sci. Data. 9, 791–808 (2017).
73. Brandt, M. et al. Satellite passive microwaves reveal recent climate-induced carbon losses in African drylands. Nat. Ecol. Evol. 2, 827–835 (2018).
74. De Grandpré, L. et al. Long-term post-fire changes in the northeastern boreal forest of Quebec. J. Veg. Sci. 11, 791–800 (2000).